
Article:
Chechik, L. orcid.org/0000-0002-7626-2694, Christofidou, K.A., Farquhar, L. et al. (3 more authors) (2023) Tools for the assessment of the laser printability of nickel superalloys. Metallurgical and Materials Transactions A. ISSN 1073-5623

https://doi.org/10.1007/s11661-023-07029-5

Tools for the assessment of the laser printability of nickel superalloys

Lova Chechik[1]*, Katerina A. Christofidou[1], Lucy Farquhar[1], Martin Tse[1], Gavin Baxter[1], Iain Todd[1]

[1]Department of Materials Science and Engineering, The University of Sheffield, Mappin Street, United Kingdom. S1 3JD

*Corresponding author – lchechik@live.co.uk

Original Research Article

Keywords

Additive Manufacturing, Printability, Weldability, Alloy Design, Nickel superalloys

Abstract

Additive Manufacturing (AM) is a revolutionary technology with great interest from the aerospace sector, due to the capability of manufacturing complex geometries and repairing of damaged components. A significant volume of research is being conducted with high-temperature alloys, particularly nickel superalloys. However, the high temperature properties of nickel superalloys are derived from the high fraction of strengthening precipitates, which in turn, lead to poor amenability to additive manufacture. Various cracking modes are common in nickel superalloys, primarily as a result of the high-level of alloying and the extreme thermal conditions experienced in AM. Herein, crack susceptibility calculations from literature were critically analysed and combined, resulting in a simple crack susceptibility index that is in agreement with literature. Currently, the range of alloys which have been tested in AM and reported in literature is limited and lacks a standard methodology, making accurate assessment of printability difficult.

Scheil solidification simulations were performed, testing solute trapping and back diffusion models for both the cooling rates associated with laser powder bed fusion (L-PBF) and laser directed energy deposition (L-DED). The results confirm that L-PBF exhibits cooling rates that can result in solute trapping, unlike in L-DED. These differences mean that alloys cannot be developed more generally for AM, but must be developed with a specific AM process in mind.

1. Introduction

Additive Manufacturing (AM), is a relatively new manufacturing technique, commonly termed 3D printing. The development of metallic AM was initiated in 1993 [1] and AM research has been increasing since; this work focusses exclusively on AM using metallic powders. The main processes which will be covered in this work are laser powder bed fusion (L-PBF) and laser directed energy deposition (L-DED); electron beam powder bed fusion (EB-PBF) will be used for comparison.

Unfortunately, not all materials can be easily printed, some materials exhibit defects such as porosity and cracking [2,3]. Therefore, for some alloys, a large processing window exists, whilst for other alloys, a successful processing window hasn't yet been found. Wei et al. defined printability as "relative susceptibilities to common printing defects" [4]. Several studies have been reported [4–6], attempting to quantify printability but no standardised experimental test for printability exists. Much work on printability is an extension upon weldability research, where weldability is defined by the American Welding Society as the capacity of a metal to be welded under fabrication conditions into a specific structure and for it to subsequently perform in its intended service [7]. Welding and the AM processes detailed are processes using a laser source to melt metal, so despite their differences, the wealth of literature published on weldability of nickel superalloys should be considered when investigating printability; this includes literature on both weldability testing [8–10] and literature focussing on nickel superalloy development/weldability [9,11–14].

Nickel superalloys are a family of alloys, originating from austenitic FCC steels [15], traditionally used in gas and aerospace turbine industries due to their exceptional mechanical and environmental properties at high temperatures [16,17]. A range of nickel superalloy compositions are shown in Table 1 along with their dominant strengthening mechanism. The first 6 of these are alloys were identified in the review by Clare et al. [18]as having decreasing printability (with Inconel 718 being the most printable), the following 3 are some of the main alloys developed specifically for AM [19,20]. The remaining alloys in Table 1 are a range of nickel superalloys, with a range of compositions as shown by the range of strengthening mechanisms and production methods.

The concept of weldability is broad, but in this work, the focus is on the susceptibility of the material to cracking. Various parameters have been developed to describe weldability, but for nickel superalloys, the alloy composition is often used as a first order approximation (Figure 1) [21,22], particularly the γ' content. By approximating weldability using the γ' content, it is assumed that strain-age cracking is the dominant mode of failure, which isn't necessarily the case (failure modes summarised in Figure 2). The first 6 alloys from Table 1 are colour coded by their printability in Figure 1 (from red to green with increasing printability), with the more printable alloys shown to be in the more weldable regions. Frequently, weldability is used as a qualitative term, alloys being referred to as having "Fair Weldability" in literature (Figure 1b). What is meant by this is that it may be possible to process the alloy under specific conditions, but the processing window might be small; resulting in failure under the wrong conditions. The label "unweldable" can be interpreted as there being no known set of processing conditions which do not result in failure [18].

The simplifications made in Figure 1 are imperfect; in Figure 1a, strain-age cracking (which often occurs in high γ' alloys) is assumed to be a good predictor of weldability. Since both Al and Ti promote γ' formation, alloys in the top right corner of the figure will be more susceptible to strain-age cracking; despite the simplicity of this plot, alloys are roughly arranged according to their printability. This is extended in Figure 1b, with a strain-age cracking susceptibility on the y-axis (approximated by a simplified γ' fraction measure) and a liquation cracking susceptibility (through carbide content) on the x-axis. Again, alloys are roughly arranged with respect to their printability, however, some alloys don't seem to follow the trend e.g., Hastelloy X has been found to crack under certain conditions [23], despite being in the readily weldable zone and ABD-900AM being printable [24], despite being above the "weldability threshold" in Figure 1a. The compositional calculations which produce these graphs

are simplistic and do not consider all defect types, they do, however, provide a rough idea of the weldability of an alloy.

Historically, improvements in mechanical properties at increased temperatures have driven nickel superalloy development. When manufacturing challenges such as solidification cracking in cast components were encountered, the alloy compositions were altered to improve their processability. An example in the field of AM is the work by Pollock et al., where two alloy compositions (Ni666 and Ni106) were designed using Thermo-Calc predictions to allow successful EB-PBF of a high γ' (70%) nickel superalloy. However, they emphasised that the solution is specific to the geometry tested and the alloy would not necessarily be printable in all geometries [25].

Table 1: List of common nickel superalloy compositions used in aerospace applications (wt %). Process shows the manufacturing process this alloy was designed for: wrought (W), cast (C), additive manufacturing (AM), powder metallurgy (PM). Strengthening mechanisms also shown: precipitation strengthened (ppt) and solution strengthened (sol)

	Cr	Ni	Co	Mo	W	Nb	Ti	Al	Fe	Hf	Ta	Cu	V	C	B	Zr	Process	Strengthening	Ref
Inconel 718	19.00	52.77	-	3.00	-	5.10	0.90	0.50	18.50	-	-	0.15	-	0.08	-	-	W/C	ppt (γ")	[16]
Inconel 625	21.50	62.95	-	9.00	-	3.60	0.20	0.20	2.50	-	-	-	-	0.05	-	-	W	sol	[16]
Hastelloy X	22.00	49.09	1.50	9.00	0.60	-	-	2.00	15.80	-	-	-	-	0.02	-	-	W/C	sol	[16]
Waspaloy	19.50	54.58	13.50	4.30	-	-	3.00	1.40	2.00	-	1.50	-	-	0.07	0.06	0.09	C	ppt (γ')	[16]
CM247LC	8.00	61.42	9.00	0.50	10.00	-	0.70	5.60	-	1.40	3.20	-	-	0.07	0.10	0.01	C	ppt (γ')	[2]
CMSX-4	6.50	64.80	9.00	0.60	6.00	-	1.00	5.60	-	-	6.50	-	-	-	-	-	C	ppt (γ')	[16]
ABD-850AM	18.68	52.50	17.60	1.89	4.74	0.60	2.22	1.29	-	-	0.44	-	-	0.01	0.03	-	AM	ppt (γ')	[19]
ABD-900AM	16.96	50.14	19.93	2.09	3.08	1.78	2.39	2.11	-	-	1.42	-	-	0.05	0.05	-	AM	ppt (γ')	[19]
AlloyDLD	19.00	64.87	4.00	4.90	1.20	3.00	-	2.90	-	-	-	-	-	0.04	0.05	0.05	AM	ppt (γ')	[20]
Rene41	19.00	55.30	11.00	10.00	-	-	3.10	1.50	-	-	-	-	-	0.09	0.01	-	W/C	ppt (γ')	[16]
In738	16.00	62.07	8.50	1.75	2.60	2.00	3.40	3.40	-	-	-	-	-	0.17	0.01	0.10	C	ppt (γ')	[16]
In713LC	12.00	72.74	-	4.50	-	-	0.60	6.00	-	-	4.00	-	-	0.05	0.01	0.10	C	ppt (γ')	[16]
Udimet700	15.00	53.37	18.50	5.25	-	-	3.50	4.25	-	-	-	-	-	0.10	0.03	-	W/C	ppt (γ')	[16]
RR1000	15.00	52.30	18.50	5.00	-	-	3.60	3.00	-	0.50	2.00	-	-	0.03	0.02	0.06	PM	ppt (γ')	[17,26]
Inconel 939	22.40	49.74	19.00	-	2.00	1.00	3.70	1.90	-	-	-	-	-	0.15	0.01	0.10	C	ppt (γ')	[17]
Haynes 282	20.00	56.34	10.00	8.50	-	-	2.10	1.50	1.50	-	-	-	-	0.06	0.01	-	W	ppt (γ')	[27]
In100	10.00	60.25	15.00	3.00	-	-	5.00	5.50	-	-	-	-	1.00	0.18	0.01	0.06	W/C	ppt (γ')	[16]
C263	20.00	50.79	20.00	5.90	-	-	2.10	0.45	0.70	-	-	-	-	0.06	-	-	W	ppt (γ')	[16]
Udimet720	17.90	55.55	14.70	3.00	1.25	-	5.00	2.50	-	-	-	-	-	0.04	0.03	0.03	W	ppt (γ')	[17]
MAR M002	8.00	60.70	10.00	-	10.00	-	1.50	5.50	-	1.50	2.60	-	-	0.15	0.02	0.03	C	ppt (γ')	[17]
ATI718+	19.00	50.21	9.00	2.80	1.10	5.50	1.75	1.45	9.00	-	-	0.15	-	0.03	0.01	-	C	ppt (γ')	[28]

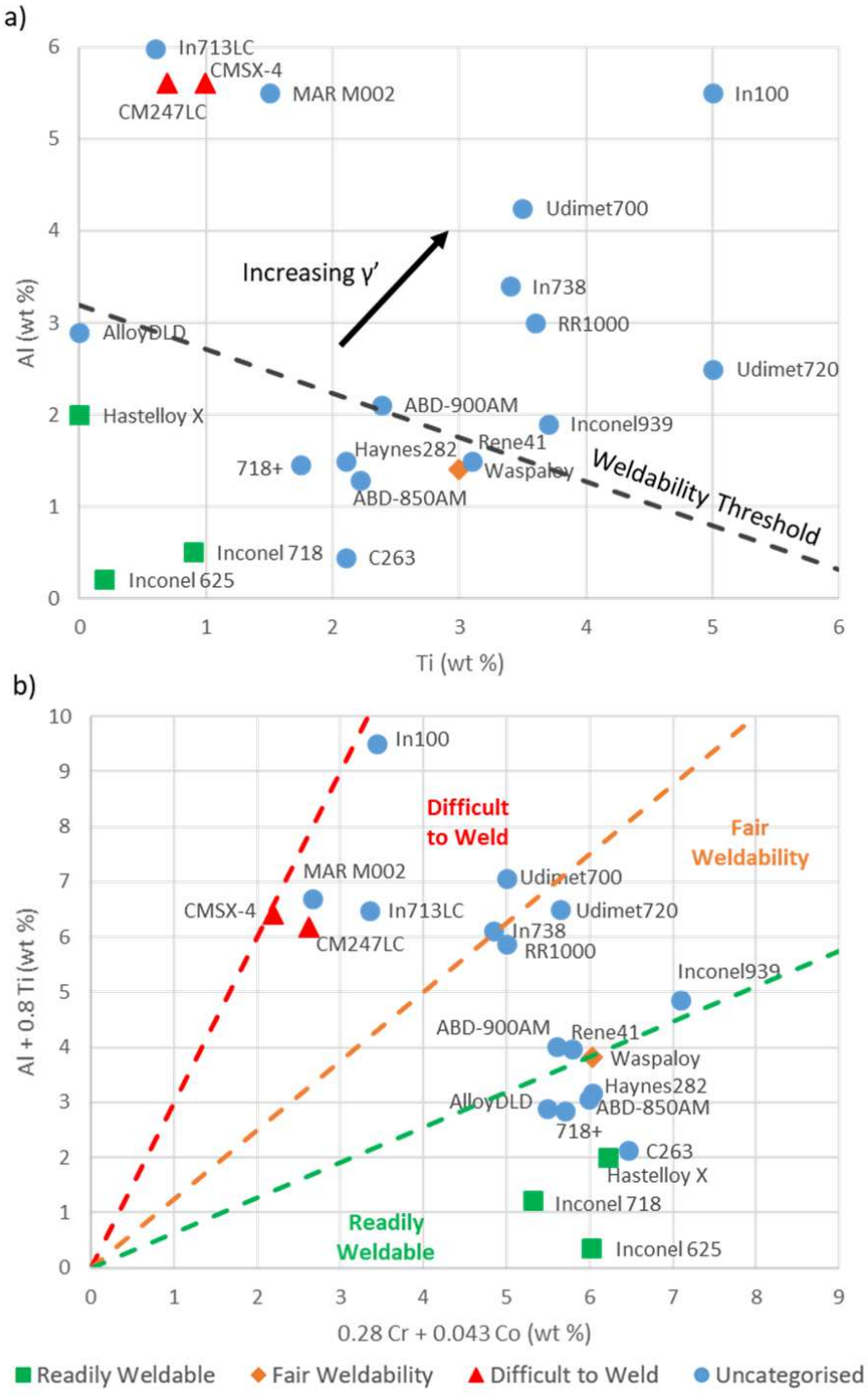

Figure 1: The dependence of weldability on composition for some common nickel superalloys. a) The dependence of weldability on Al and Ti for some γ' strengthened superalloys. Reported by Illston, where strain-age crack susceptibility is being used as a weldability indicator [29] *b) A different method of calculating weldability using composition. Reported by Haafkens and Matthey* [30]*. Printability of alloys to be analysed is colour-coded, with green being easily printable, red being not printable, orange being somewhat printable (defined by Clare et al.), and blue being alloys not mentioned by Clare et al.* [18]

Generally, the aim is to create a printable alloy, with an appropriate balance of properties for industrial applications e.g. turbine blade repairs. To design alloys tailored to AM, the common failure mechanisms encountered during manufacturing processes need to be understood and criteria developed to address them during the design process. There are many forms of failure associated with metallic components, the ones selected below are particularly applicable to nickel superalloys. Some of these occur during solidification while others occur during heat treatment; solidification cracking is frequently thought of as being the biggest issue in AM of nickel superalloys [12,31,32]. Other cracking mechanisms in AM of nickel superalloys are explored in detail in the review by Markanday [3].

In nickel superalloys, the dominant failure modes are briefly outlined below and shown diagrammatically in Figure 2 [22,33,34]:

Solidification Cracking (Hot Tearing)

Solidification cracking occurs in the later stages of solidification, where dendrites are interlinked within the mushy zone [2]. This means that shrinkage due to solidification cannot be filled from the remaining liquid, creating an intergranular crack [18,35,36]. This complex process is dependent on both the composition of the final liquid and on the cooling rate during the late stages of solidification. This has led to there being two distinct ways of predicting solidification cracking [37]:

- Metallurgical models, which use solidification curves and critical temperature ranges (based on phase diagrams) [37]
- Thermo-mechanical models, which look at the solidification in terms of strains, strain rates and stresses associated with the shrinkage [37,38]

The former is a simpler analysis, which was developed in the 1970s [37], assessing solidification from a global perspective, as exemplified by the crack susceptibility coefficient, developed by Clyne and Davies [39]. The latter focusses more on the mechanism during the final stage of solidification and wasn't properly explored until the 1990s. More complex calculations are involved, e.g. the critical strain rate developed by Rappaz, Drezet and Gremaud, often referred to as the RDG model [40] and a the Kou cracking susceptibility coefficient [35]. Since solidification cracking is mainly a product of segregation [32], the smaller melt pool in AM (as compared to welding) means that the propensity of alloys to solidification cracking in AM is reduced.

Liquation Cracking

Liquation cracking is similar to solidification cracking, but occurs when the bulk has already solidified. Low melting point phases e.g. grain boundary carbides or the γ/γ' eutectic remelt at temperatures below the melting point (T_m) of the bulk [2]. This often occurs in welding behind the main bead; the weld heats up the grain boundary phases, creating molten pockets along the boundary in the heat affected zone (HAZ). The tensile stress due to the weld can be sufficient to tear the grain boundary, creating a liquation crack, also known as a HAZ fissure [34]. There is a fine composition balance; carbides are desirable for improving mechanical properties, yet this change in composition can decrease the melting point of the final solidification composition due to the γ/γ' eutectic [2,41]. In an attempt to improve mechanical properties, susceptibility to liquation cracking can inadvertently be increased; since the carbide content affects liquation cracking, the susceptibility can be calculated based on the compositions of the alloys [21]. Similarly to solidification cracking, the smaller melt pool size in AM tends to decrease susceptibility to liquation cracking when compared to welding.

Strain-Age (Reheat) Cracking and Ductility Dip Cracking

Both strain-age and ductility dip cracking occur below the solidus temperature (0.4-0.9 T_s) in precipitate strengthened superalloys. Post solidification, components are heat treated to relieve residual stresses, this however has the side-effect of allowing γ' precipitates to precipitate and coarsen. The precipitation often occurs before the relaxation and increases the yield stress, reducing ductility. This means that material is still highly stressed, but is now more brittle and allows the initiation of strain-age cracks [42]. Strain-age cracking can be

related to the γ' content, the composition and corresponding volume fraction of which can be estimated, so γ' volume fraction can be estimated. Al, Ti, Ta, Nb and Hf are the main γ' forming/strengthening elements [16,17]; various equations exist to calculate a susceptibility to strain-age cracking from the expected volume fraction of γ' [19,41].

Ductility dip cracking (DDC) occurs in the same manner, but here the carbides on the grain boundaries coarsen and act as stress concentrators. Cracks can often occur along these lines of carbides following the grain boundaries, resulting in DDC [43]. Both cracking mechanisms are fundamentally caused by precipitation; if an alloy is over-aged before processing, the ductility is increased and strain-age cracking minimised [34,44].

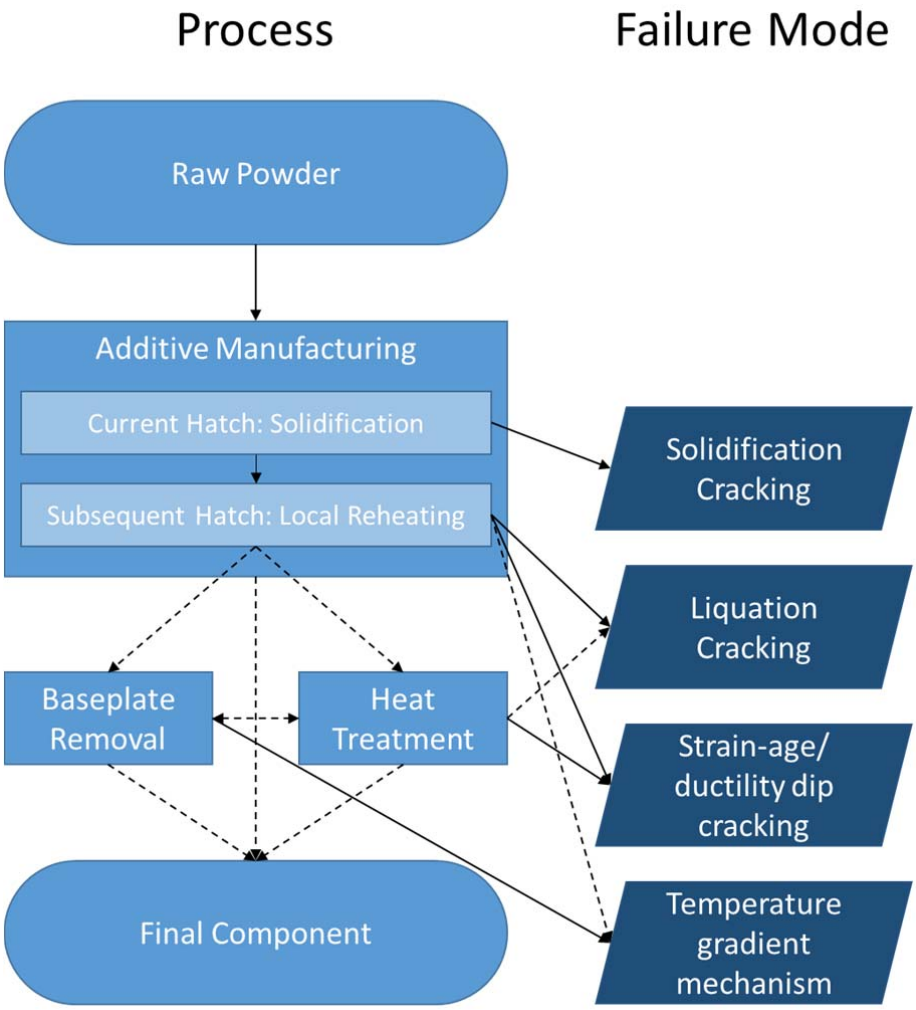

Figure 2: Flow-chart correlating dominant failure modes with the processing stage at which they occur, dotted lines represent less frequent occurrences

1.1. Imposed Conditions in Additive Manufacturing

The thermal history during the AM process is much more complicated than that of conventional manufacturing methodologies and includes some of the following considerations:

1. Laser heats localised area to above the melting point

2. Conduction from the melt pool creates a HAZ
3. As the laser moves, the large thermal mass of unmelted material causes the melted region to solidify rapidly
4. The subsequent layers remelt the original region
5. Once the laser is further away (subsequent hatches), this region is reheated with subsequent heating cycles

The small size of the melt pool means that the cooling rates are much higher than in processes such as welding, casting or powder metallurgy. Cooling rates for L-PBF are reported as ~10^5-10^6 K/s and L-DED as ~10^3-10^4 K/s, these are both much faster than common manufacturing processes e.g. casting [45].

If the solidification velocity is very high, this is known as rapid solidification (chemical equilibrium is not reached) and can cause solute trapping when the solidification front moves quicker that the solute atoms can diffuse in the liquid state. The speeds needed to achieve rapid solidification are said to be on the order of 10^{-2} m/s for localised diffusion and ~1 m/s for complete solute trapping [46].

Typical velocities in the L-PBF process are on the order of 1 m/s, so are on the boundary of solute trapping, but L-PBF is frequently assumed to occur under rapid solidification conditions. Since L-DED is a slower process, with typical velocities of ~ 10^{-2} m/s, the process is on the cusp of rapid solidification. This suggests that diffusion may occur in L-DED, which is not present in L-PBF.

1.2. Alloy Design

Currently, the majority of alloys used in AM are designed for conventional manufacture [25]. However, efforts are now being undertaken to design alloys tailored to AM, and as such, discussions of "printability" are paramount. Several parameters have been developed, such as:

$$\text{Stress Performance Index, } \sigma = \frac{E\alpha_{CTE}}{2\kappa(1-\nu)}$$

Equation 1 [47,48]

where E, Young's Modulus; α_{CTE}, thermal expansion coefficient; κ, thermal conductivity; ν, Poisson's ratio.

$$\text{Thermal Strain Parameter, } \varepsilon^* = \frac{\beta\Delta T}{EI}\frac{\sqrt{Vl}}{\kappa\sqrt{\rho}}H^{3/2}$$

Equation 2 [5]

where β is the volumetric thermal expansion coefficient; ΔT is the temperature range (peak to surroundings); I, the second moment of inertia; V, the melt pool volume; l, the layer thickness; ρ, the density and H the heat input per unit length $\left(\frac{Absorptivity \times Power}{Velocity}\right)$ [5].

These coefficients are dependent on both material properties and the processing conditions, so may be more suitable to the minimisation of thermal strain of a specific alloy (by varying processing conditions) than for alloy design.

PHACOMP (PHAse COMPutation) is a calculation, developed in the 1960's to predict the propensity of topologically close packed (TCP) phases in nickel superalloys by approximating the composition of the final γ matrix [16,49]. The susceptibility to form TCP phases (e.g. σ, μ) can be calculated [50] by combining the electron vacancy numbers for each element.

There are some interesting interplays at work, so finding an optimal composition is not easy; if the amount of γ'' is increased, this reduces the susceptibility to strain-age cracking, but increases the likelihood of solidification cracking and liquation cracking [22]. For EB-PBF, alloy compositions have been altered to allow better control of the columnar to equiaxed transition through processing parameter manipulation, albeit only for a specific geometry in the EB-PBF process [51].

Further publications have investigated the design of new nickel superalloys [52–54], with some specifically for AM [55–57]; most notably Tang et al. (Alloyed), [19] Conduit et al [20], Smith et al. and Pollock et al. The first two of these used complex computational methods to calculate properties of large numbers of alloy compositions; a summary of computational techniques used for alloy design is reported by Markanday [3]. Besides indices indicating printability factors, mechanical properties, cost and weight were also considered. Additionally, Wahlmann et al. defined 4 different cracking criteria, and designed an alloy composition trying to reduce each crack susceptibility individually; unfortunately cracking remained in all the new alloys [31].

Tang et al. designed a "medium γ' fraction" alloy (ABD-900AM), i.e. < 50 %, to be compared with CM247LC and Inconel 939 and tested this using L-PBF [19]. The freezing range was utilised as a simple indicator of solidification cracking, with the Kou cracking susceptibility [35] trusted more than the RDG model. However, the Kou methodology was used over a different solidification interval, $0.10 > f_L > 0.01$ (where f_L is the liquid fraction), compared to that used by Kou of $0.13 > f_L > 0.06$ [19,35]. Additionally, both creep life and strain-age cracking scale with γ' content, resulting in a compromise between maximising creep life whilst avoiding cracking.

Conduit et al. considered similar criteria for their alloy selection, however, the alloy designed through this methodology was specific for L-PBF [20]. In this approach, previously known materials parameters were used and a neural-network created to extrapolate factors such as 'processability' between them – albeit no details of the processability scale were given. Further, CALPHAD (CALculation of PHAse Diagrams) calculations were performed using Thermo-Calc [58] to estimate both the γ' content and the overall phase stability. The final alloy was gas atomised [20] and tested using L-PBF, resulting in the predicted properties. However, the alloy was given a 30% chance of fulfilling the requirements, concluding that there is much still unknown about alloy development.

Studies comparing solidification cracking criteria reach different conclusions as to the best criterion to use; Ghoussoub et al. begin by using the freezing range to screen for new alloys, but then use the RDG and an adjusted Clyne and Davies model to yield more accurate results [59]; it was noted that cracking density varied with distance from the component edge. Other nickel superalloy design projects primarily aim to minimise the freezing range [60–62], by removing elements (e.g. Hf) [60] or adjusting compositions [61]. Several other criteria have been considered, including the γ/γ' lattice misfit [62,63] and a heat/deformation resistance model which assumes that the final microstructure is a composite consisting of dendrite cores and the interdendritic regions [61]. Park et al. reduced the cracking in a high γ' alloy by replacing Ti with Ta, this increased the freezing range and the γ' content (contrary to Thermo-Calc predictions), the reduced cracking was attributed to the improved powder flowability [63].

Yu et al. report a thorough comparison of solidification cracking and strain-age cracking criteria, proceeding to select alloys using only the two measures which they found to be most accurate [64]. One of these is the freezing range, whose reliability is debated over in literature [19,63]; the remaining criteria are discarded and so have no influence on the final result. 3 alloy compositions are selected but not experimentally tested [64]; since the accuracy of each crack susceptibility index is unknown, selecting 2 and discarding the others may not be the optimal way of approaching this issue.

In this paper, a critical analysis of cracking susceptibility is performed, comparing the results with printability for both L-PBF and L-DED. Several cracking criteria are combined to develop an overarching failure susceptibility index, which is then compared to the reported printability of nickel superalloys from literature. Calculations are purposefully kept simple, reducing the barrier for integration; multiple calculations are performed for each failure mode to capture a greater variety of potential failure mechanisms. Furthermore, advanced Scheil simulations were compared for L-PBF and L-DED to determine the accuracy of these models and highlight the differences expected between the two AM processes.

2. Methods

2.1. Solidification Calculations

2.1.1. *Thermo-Calc*

Thermo-Calc 2021b was used to perform classic Scheil solidification simulations of the 21 alloy compositions listed in Table 1 from their liquidus to 99.5% solid [58]. Thermo-Calc recently added the capability to perform Scheil solidification simulations taking into account either back diffusion or solute trapping. Solidification with back diffusion allows for diffusion in the primary solid phase and requires a cooling rate to be inputted. Solidification with solute trapping allows for one phase to form in which solute trapping can occur due to high solidification speeds (which are used as an input). Laser scanning velocities were used as the solidification speeds [5]. TCNI8 and MOBNI4 databases were used for thermodynamic properties and element mobility (for back diffusion) respectively.

For L-DED, a cooling rate of $5x10^3$ K/s was used with a scanning speed of 0.04 m/s (2400 mm/min). For L-PBF, a cooling rate of $1x10^6$ K/s was used with a scanning speed of 1 m/s. Further Scheil calculations were performed for the first 9 alloys in Table 1 (the first 6 being commonly used in AM as reviewed by Clare et al. [18], the latter 3 being alloys specifically designed for AM [19,20]); for each of these, both back diffusion and solute trapping calculations were performed for both L-DED and L-PBF conditions. By testing these new calculations, we can determine whether the altered Scheil calculations affect the resultant crack susceptibilities.

From the solidification curves, several values were extracted and calculated:

- Liquidus temperature, used for viscosity calculations
- Freezing range ($0.01 < f_L < 0.99$ used)
- Crack Susceptibility Coefficient, calculating the ratio of the vulnerable time ($0.01 < f_L < 0.1$) to the relaxation time ($0.1 < f_L < 0.6$) [39], assuming a constant cooling rate, so times can be replaced with temperature ranges
- Kou Cracking Susceptibility [35], $\left|\frac{dT}{d({f_L}^{0.5})}\right|$ for the range $0.06 < f_L < 0.13$

2.1.2. *New PHACOMP*

TCP phases are avoided where possible in nickel superalloys, particular the σ phase. Using atomic compositions, the carbon is allocated to form MC and $M_{23}C_6$ equally, the boron to form M_3B_2 and then γ' to form (Ni_3M). The remaining elements form the atomic composition of the final γ matrix, so this can be used to calculate an average electron vacancy number.

$$N_v^{ave} = \sum_{i=1}^{n} X_i (N_v)_i$$

Equation 3

Where N_v^{ave} is the average electron vacancy number, X_i is the atomic fraction of the element in the γ matrix, n is the number of elements present and N_v is the electron vacancy number of the specific element [65].

In 1984, Morinaga et al. developed a new alternative, named "New PHACOMP" [66]. A similar process was followed, but using metal d-levels (M_d), which correlate with electronegativity and are listed in the original paper [66]. This was performed on the measured γ composition.

$$M_d^{ave} = \sum_{i=1}^{n} X_i (M_d)_i$$

Equation 4

The phase allocations performed for PHACOMP [65] assumes precipitates are fully formed using up the maximum amount of solute possible; since this is unlikely to occur in reality, "New PHACOMP" was calculated using both the initial composition of the alloy and the γ composition as calculated once all other phases were formed.

2.2. Composition-based Calculations

Three other simple calculations were performed, based on the compositions of the alloys by weight. The first two estimate the relative γ' prevalence (similarly to Figure 1b), as a higher fraction of precipitates would reduce ductility and promote strain-age cracking. The third estimates the carbide prevalence, as more carbides could lead to increased liquation cracking (as in Figure 1b).

1. $M_{Al} + 0.84M_{Ti}$ [41]
2. $M_{Al} + 0.5M_{Ti} + 0.36M_{Nb} + 0.15M_{Ta}$ [19]
3. $0.28M_{Cr} + 0.043M_{Co}$ [30,41]

Where M_i is the weight fraction of the element

Figure 3 shows comparison between calculation 2 (above) and the Thermo-Calc prediction of equilibrium γ' composition (at 700 °C). There is a strong positive correlation ($R^2 = 0.95$).

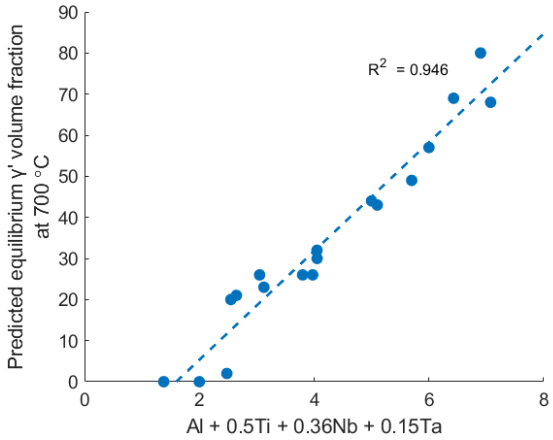

Figure 3: Comparison of two calculations for γ', a simple compositional analysis (reported by Tang et al [19]) against the equilibriums volume fraction predicted by Thermo-Calc

2.3. Physical Property Calculations

Since the critical strain during solidification is inversely proportional to viscosity (RDG model) [40], a high viscosity is expected to be indicative of a large hot crack susceptibility. For each alloy, a viscosity was calculated at the liquidus temperature (as calculated by Thermo-Calc); this was done by combining viscosities of various binary nickel alloys as published by Sato [67,68]. Formulas for A and B coefficients for key elements were given in the paper, but with errors in notation, the following are the determined to be the correct equations:

$$\ln \mu_{alloy} = \Sigma C_i A_i + (\Sigma C_i B_i) \frac{1}{T_L}$$

Equation 5

$A_{Co} = -0.607 - 0.06\ C_{Co}$	$B_{Co} = 2.20 - 0.20\ C_{Co}$
$A_{Cr} = -0.616 - 0.44\ C_{Cr}$	$B_{Cr} = 2.23 - 0.55\ C_{Cr}$
$A_{Al} = -0.609 - 0.11\ C_{Al}$	$B_{Al} = 2.22 - 0.75\ C_{Al}$
$A_{W} = -0.583 - 2.28\ C_{W}$	$B_{W} = 2.17 - 7.00\ C_{W}$
$A_{Ta} = -0.598 - 3.04\ C_{Ta}$	$B_{Ta} = 2.17 - 8.98\ C_{Ta}$

where T_L is the liquidus temperature (K) and C_i is the atomic fraction of the element when excluding nickel, $C_i = C_i / (1 - C_{Ni})$ [67]. Where there were elements present which were not in this list, coefficients of the element with the nearest melting point were used [67], resulting in the following coefficients being used for the following elements. Co parameters for Co, Ti, Fe, Cu. Cr parameters for Cr, Hf, V, B, Zr. Al parameters for Al only. W parameters for W and C. Ta parameters for Ta and Mo.

2.4. Combination of Cracking Susceptibilities

The following 10 susceptibilities have been categories into four failure modes (FM) as described above.

1. FM1: Solidification Cracking
    a. HT1: Crack Susceptibility Coefficient
    b. HT2: Freezing Range (K)
    c. HT3: Kou Cracking Susceptibility (K)
    d. HT4: Viscosity (mPa·s)
2. FM2: TCP Phases
    a. TCP1: PHACOMP on γ composition
    b. TCP2: “New PHACOMP” on γ composition
    c. TCP3: “New PHACOMP” on bulk alloy composition
3. FM3: Strain-age cracking
    a. SAC1: $M_{Al} + 0.84M_{Ti}$
    b. SAC2: $M_{Al} + 0.5M_{Ti} + 0.36M_{Nb} + 0.15M_{Ta}$
    c. SAC3: Volume Fraction γ’ (at 700° C)
4. FM4: Liquation cracking
    a. LC1: $0.28M_{Cr} + 0.043M_{Co}$

Each of these 10 individual susceptibilities was normalised between 0 - 1, with 0 being least failure susceptible, 1 being most failure susceptible, with the exception of viscosity, for which a value of 0 would denote the less processable material. For each failure mode, a root mean square was calculated from the individual susceptibilities, this gives each alloy a single score for each failure mode – again ranging between 0 - 1. Root mean square was chosen as a method of combining independent susceptibilities, giving the higher susceptibilities more weight. These 4 failure modes were combined using root mean square (as above), resulting in a single overall failure susceptibility score for each alloy.

3. Results

3.1. Cracking Susceptibilities

The individual susceptibilities for each of the four failure modes and the overall susceptibility are both summarised in Table 2. The overall susceptibilities are plotted in Figure 4 for the 9 alloys chosen to represent common AM superalloys and alloys designed specifically for AM; envelopes show the failure susceptibility of the highest/lowest failure mode for that alloy, from Table 2.

It can be seen that Inconel 718 and Inconel 625 both have low overall failure susceptibilities, which corresponds with literature, in which they are widely reported. Hastelloy X is expected to be a fairly printable, but exhibits a relatively high overall failure susceptibility. CM247LC, CMSX-4 and Waspaloy are all expected to be difficult to print as reflected by the high overall failure susceptibility. Finally, the 3 alloys designed for AM all have fairly high susceptibilities, with AlloyDLD being the lowest.

Table 2: Normalised susceptibilities for the 4 failure modes for each of the 21 alloys and the overall failure susceptibility for

Alloy	FM1	FM2	FM3	FM4		Overall Susceptibility
Inconel 718	0.39	0.35	0.14	0.64		0.42
Inconel 625	0.40	0.23	0.00	0.78		0.45
Hastelloy X	0.55	0.82	0.15	0.82		0.65
Waspaloy	0.50	0.34	0.39	0.79		0.53
CM247LC	0.56	0.52	0.87	0.09		0.58
CMSX-4	0.39	0.38	0.92	0.00		0.53
ABD-850AM	0.54	0.22	0.31	0.77		0.55
ABD-900AM	0.55	0.44	0.47	0.70		0.50
AlloyDLD	0.41	0.30	0.38	0.67		0.57
Rene41	0.60	0.65	0.41	0.73		0.62
In738	0.50	0.56	0.75	0.54		0.61
In713LC	0.46	0.49	0.96	0.24		0.72
Udimet700	0.72	0.90	0.85	0.57		0.69
RR1000	0.56	0.76	0.69	0.57		0.71
Inconel939	0.46	0.65	0.53	1.00		0.53
Haynes282	0.33	0.45	0.31	0.78		0.68
Udimet720	0.27	0.84	0.72	0.70		0.51
718+	0.39	0.54	0.39	0.72		0.42

each alloy

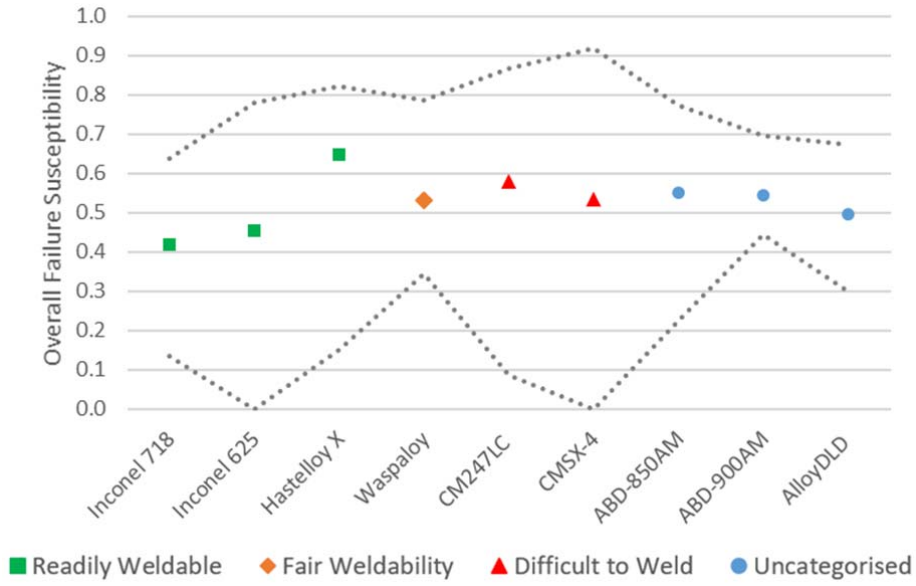

Figure 4: Overall failure susceptibilities of the main alloys being analysed. Envelopes show the failure susceptibility of the minimum/maximum failure mode for that alloy. Colour coding continued from weldability plots in Figure 1, 3 new alloys have no known weldability, so are coloured blue

3.2. Thermo-Calc Scheil Calculations

To analyse the effect of non-equilibrium Thermo-Calc simulations on the susceptibility coefficients, Scheil calculations were performed on 9 alloys with 5 different conditions. The three models used were the classic calculation (no solid diffusion); back diffusion (BD) in the primary solid phase allowed (this was performed using both L-PBF and L-DED cooling rates); and solute trapping (ST) in the primary solid phase (performed using both L-PBF and L-DED scanning velocities).

To quantify the change between different conditions, each of the three outputs of the Thermo-Calc calculations (HT1, HT2, HT3) are shown in Figure *5*. The freezing range (Figure *5*b) of the ST PBF is noticeably lower than the other calculations, the BD DED is also slightly lower – the rest of the calculations gave the same results. A similar trend was seen in the Kou cracking susceptibilities (Figure *5*c), with ST PBF being noticeably lower throughout but with no other clear trends visible. The CSC (Figure *5*a) results are more variable. ST PBF deviated the most from the trend, with the others closely aligned to the classic Scheil results with some minor anomalies.

To quantify this, for each alloy, the percentage difference between the condition and the classic Scheil was calculated, and are summarised in Table 3. For example, if solute trapping was consistently different to the classic Scheil, we could deduce that Thermo-Calc predicts solute trapping to be significant under those conditions. An average of these deviations (absolute values) for each condition across all 9 alloys was taken (Table 3). ST PBF had the largest average deviation value for each output, as expected from the plots in Figure *5*. These deviations were averaged over all 3 outputs; the ranking being ST PBF, BD DED, ST DED and finally BD PBF. This suggests that Thermo-Calc predicts solute trapping to be significant in PBF and that in DED, back diffusion is more significant than solute trapping.

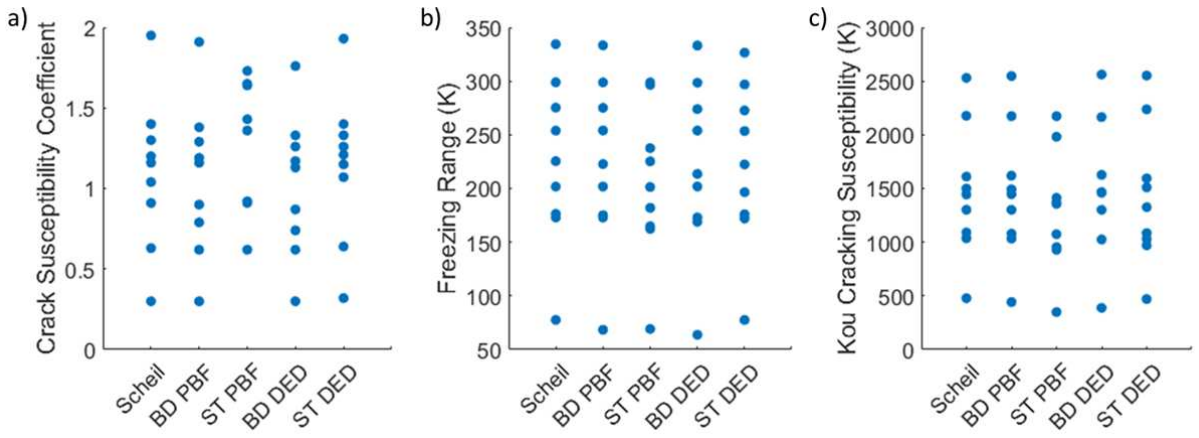

Figure 5: Comparison of 5 different Thermo-Calc Scheil calculations for 9 alloys a) Crack Susceptibility Coefficient*, b)* Freezing Range*, c) Kou Cracking Susceptibility*

Table 3: Average variation between various Scheil calculations when compared to the classic Scheil calculation; percentages reported as decimals. BD denotes back diffusion, ST denotes solute trapping

	Average of Absolute Percentage Differences from classic Scheil			
Calculation	Crack Susceptibility Coefficient	Freezing Range	Kou Cracking Susceptibility	Overall Average
BD PBF	0.032	0.016	0.012	0.020
ST PBF	0.375	0.088	0.137	0.200
BD DED	0.064	0.031	0.036	0.044
ST DED	0.063	0.010	0.048	0.040

4. Discussion

4.1. Combining Crack Susceptibility Criteria

In this work, no new models were introduced, instead, the various causes of defects and cracks were quantified using as simple a method as possible. As mentioned previously, Wei et al. define printability as "relative susceptibilities to common printing defects" [4]. Here the focus is solely on printability, ignoring the materials properties (which must be sufficient for aerospace accreditation), cost and density, which previous works include [19,20]. These previous attempts use complex, computationally intensive methods to extrapolate between known compositions and use neural networks. This complexity stops the method from being easily available to the wider research community.

Herein, previously published equations, mainly based upon the alloy compositions are utilised, coupled with CALPHAD calculations, a tool routinely used within the community. The first 6 alloys in Table 1 are roughly presented in printability order; Inconel 718 and Inconel 625 are both widely reported as being printable with good properties in L-PBF, EB-PBF and L-DED [18]. Hastelloy X has been widely printed using L-PBF, somewhat printed in L-DED and EB-PBF – this doesn't necessarily mean that it's more difficult to print using these processes, but simply that few L-DED/EB-PBF studies have been reported in the wider literature [18]. In an ideal

situation, a standardised printability measure would be developed, allowing direct comparison between many alloys, even if only few studies existed. Currently, due to the lack of standardisation, inclusion of less-reported alloys increases uncertainty in this analysis.

The equilibrium γ' content of each alloy (as calculated using Thermo-Calc) is a proxy of strain-age cracking, and the crack susceptibility coefficient is a measure of solidification cracking. Both were calculated using Thermo-Calc and are shown in Figure 6. Effectively, this is an extension to the plots seen in Figure 1, as widely reported in literature [21,29,41]; alloys appear to cluster by their weldability/printability. Both axes use results calculated by Thermo-Calc for direct comparison, but the γ' fraction calculated using Thermo-Calc has been shown to be strongly correlated with that using the alloy composition (Figure 3). Despite the strong correlation shown in Figure 3, 3 different calculations were combined for FM3 (strain-age cracking), two composition based and one from Thermo-Calc. Since it is unknown which is the most accurate and by combining the different calculations, the effect of anomalous results should be minimised. FM3 calculations are based on γ' composition; some alloys (e.g. Inconel 718) are γ" strengthened, but these are the minority as seen in Table 1, so the calculations focus on γ' strengthened alloys.

The overall failure susceptibilities (Figure 4) should inversely correlate with printability. The lowest failure susceptibilities are for Inconel 718 and Inconel 625 which align with them being the most printable alloys, implied by the fact that they're widely reported in literature. Waspaloy seems to be relatively printable, but with minimal literature published [69–71]. AM of Waspaloy has been attempted in L-PBF and L-DED and seems to have been built successfully with each, but with minimal research interest, so few further publications are available. This has a much higher overall failure susceptibility than Inconel 718 or Inconel 625, but lower than that of CM247LC and Hastelloy X.

CM247LC and CMSX-4 are both notoriously hard to print, but are of great industrial relevance due to their high-temperature applications e.g. in turbine blades. This disproportionate research interest may make these alloys seem more printable than they are; the overall failure susceptibility of CM247LC is very high as expected, but that of CMSX-4 is lower – it has a very high susceptibility to strain-age cracking, but this is lost in the overall susceptibility due to the relatively low susceptibilities to the other 3 failure modes. Finally, Hastelloy X is relatively printable according to literature, but scores very highly on the overall failure susceptibility. This is due to it having two failure modes of susceptibilities around 0.8 – these are high enough to bring its' overall susceptibility to above that of CMSX-4. Looking at the maximum failure mode, shown in Figure 4, it can be seen that this is greater for CMSX-4 than for Hastelloy X. Hastelloy X is a solid solution strengthened alloy (Table 1), which may explain the different behaviour of this alloy.

Clearly the combination of the overall failure susceptibility from the four failure modes isn't perfect, but overall the correct trend is seen. It's impossible to quantify the printability of an alloy – especially due to the fact that some alloys may be more printable in one process than another e.g. printable using EB-PBF, but not using L-PBF. Attempts of quantifying printability have resulted in a stress performance index [47] and a thermal strain parameter [5], both of which require materials properties such as expansion coefficients and the Young's modulus, which can't be accurately obtained before the material exists. Additionally, the latter uses the processing parameters as inputs, so is looking at the likelihood of a build failing rather than the overall printability of an alloy.

The inherent complexity of AM makes this all the more difficult. Not only is there variation within a component, with heat often accumulating with build height, heat can also accumulate within a layer due to short return times. Calculating a thermal strain parameter for a specific material and set processing parameters would give a single value, but this would vary with geometry, so ideally, a geometric factor would also be needed. Finally, even if it were possible to integrate geometry, the cooling rate and solidification velocity vary within the melt pool. So even if the centre of the melt pool was resistant to a certain form of failure, the edge of the melt pool could experience conditions which could cause cracking. Due to this complexity, printability values should be

taken as qualitative values to compare relative crack susceptibility – in an attempt to generally minimise propensity of cracking.

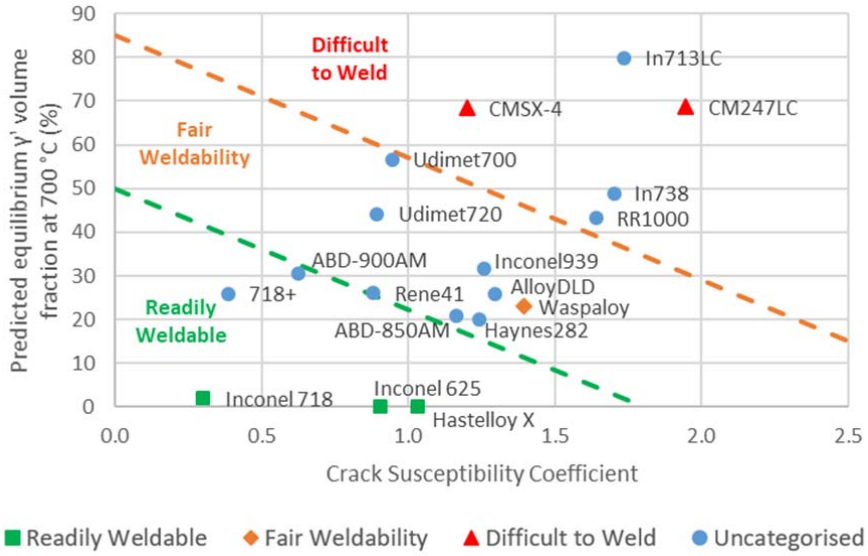

Figure 6: Plot showing the relationship between γ' content and the crack susceptibility coefficient, both calculated using Thermo-Calc

Most alloy compositions are given as an allowable range e.g. [28], but all calculations above were performed on a specific composition. This naturally introduces error into the calculations, as some elements have a 4 wt.% allowable range. The difference is likely to be larger in the Thermo-Calc calculations, as the final solidification path is very sensitive to composition. PHACOMP is calculated on the calculated final γ composition, where all other phases are assumed to have fully precipitated (γ' and carbides) [16,65]. Due to the rapid solidification experienced in AM, precipitation is limited due to the reduced time for diffusion. The composition of the actual γ phase is expected to be between the original alloy composition and that calculated by PHACOMP (calculated using AS5491 [65]). Since the cooling rate in the L-PBF process is higher than in L-DED, less segregation is expected, so the γ composition is likely to be closer to that of the powder than during L-DED.

Combination of susceptibilities was done using the root mean square, this was chosen as a way of maintaining the normalised nature of results whilst giving the larger susceptibilities a heavier weighting. This means that four scores of 0.25 would rank lower than a 1 and three scores of 0; if the susceptibilities were summed, these would be equal. Despite the imperfect results, the general trend from literature is followed. Each susceptibility within a failure mode is weighted equally, the accuracy of these susceptibilities is not known, and hence it is assumed that combining them all will help remove any anomalous results. The susceptibilities of the four failure modes are also weighted equally, as they are combined using a root mean square. Some failure modes are likely more prevalent than others, but since a single alloy can experience different failure modes under different conditions, it was decided to include all of the failure modes.

The different calculations used for solidification cracking are compared in Figure 7. A positive correlation is shown between the Clyne Davies and RDG models (Figure 7a). This level of scatter is similar to similar plots reported in literature [64]. It is reassuring to see that simple models seem to be able to equal the performance of more complex ones. Figure 7b shows the positive correlation between freezing range and the Kou susceptibility [35], this shows a stronger correlation that Figure 7a. There are some unexpected results e.g. CMSX-4 and CM247LC both showing relatively low susceptibilities. However, the freezing range has widely been used as a proxy to solidification cracking susceptibility so the accuracy of the Kou could be questioned.

Figure 7c shows the Kou susceptibility against the RDG model, one from each of the previous plots. There is a weaker positive correlation between these. However, the general trend still remains; since we do not have accurate experimental results to compare solidification cracking susceptibility to, all 4 measures are calculated. Since a root mean squared of these is taken, if an alloy has a high susceptibility according to one measure, this should be carried into the overall normalised solidification cracking susceptibility; this allows all the criteria to be considered, rather than relying on a single criterion, which tends to be the case in literature.

An argument could be made that FM2 (TCP phases) should be removed, as this results in poor mechanical properties rather than process failure. An adjusted failure susceptibility has been plotted in Figure 8, excluding FM2. This drops the susceptibility of Hastelloy X, bringing it closer to reports from literature, CM247LC and CMSX-4 both remain high as expected. Waspaloy still has a high score, due to being fairly susceptible to two failure modes as explained previously.

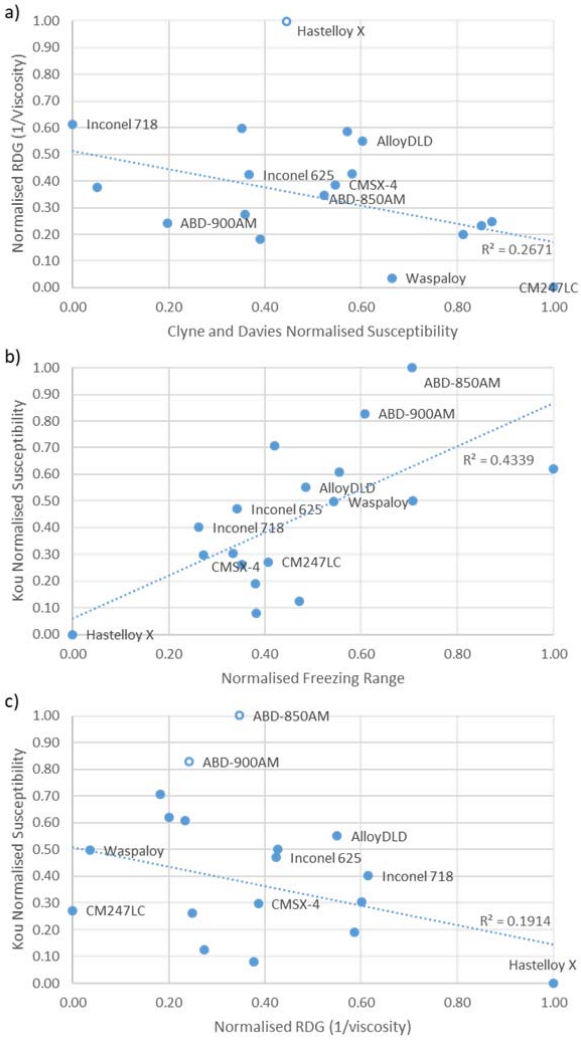

Figure 7: Comparison between various solidification cracking susceptibilities. a) RDG vs Clyne and Davies, b) Kou vs Freezing Range, c) Kou vs RDG. Anomalous points unfilled

For some of the susceptibility parameters, there are arbitrary thresholds given in literature. E.g. Morinaga et al. observed that alloys which are σ-prone tend to have M_d values above 0.915 [66]. An approach of blindly discarding

any alloys above this threshold could be taken, but this seems to be an observation without any scientific reasoning. Instead, 21 alloys were selected, to cover as wide a range of compositions as possible. The idea is that this results in a more accurate susceptibility score. If we only analysed the first 6 alloys, they could all have similar scores on one failure mode, so the highest would be given a large normalised failure susceptibility – whereas when considering a more global perspective, they could all be of low failure susceptibility.

The crack susceptibility calculations are purposefully simple and require minimal computational intensity. The results have significant scatter, but their accuracy is comparable with those in literature and appear to adequately reflect printability rankings. There is a large amount of uncertainty in the process; the composition of the alloy could be variable, the thermal conditions vary within the melt pool and across the component. These uncertainties limit the overall accuracy of the model, but should still allow a rough ranking of alloy printability. Realistically, so little is known about the actual printability of alloys, that this becomes the limiting factor. Various printability factors can be calculated, but there is no standardised method for measuring printability and very few alloys have been manufactured using AM. There needs to be a defined measure of printability to compare crack susceptibilities to before the efficacy of crack susceptibilities can be thoroughly assessed.

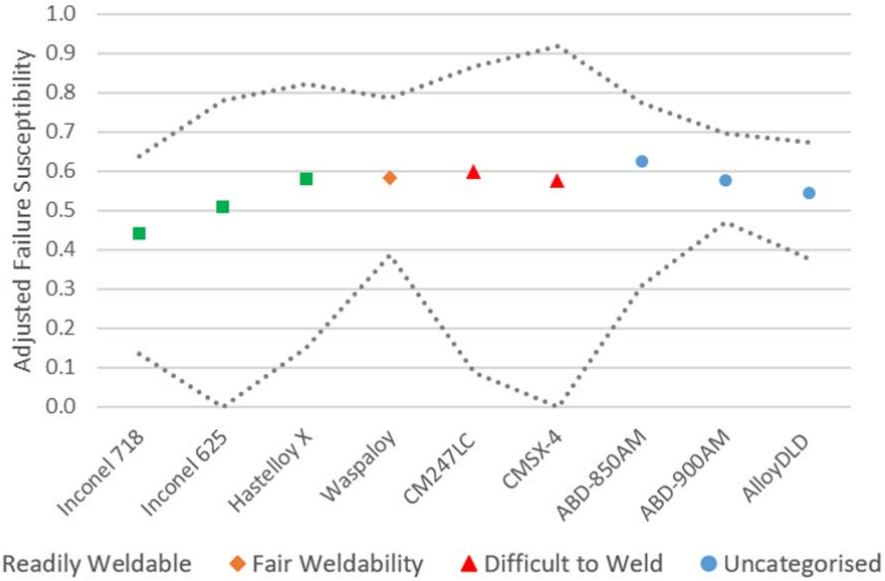

Figure 8: An adjusted failure susceptibility of the main alloys being analysed, excluding FM2. Envelopes show the failure susceptibility of the minimum/maximum failure mode for that alloy.

4.2. Thermo-Calc Scheil Solidification Simulations

Solidification cracking susceptibilities (FM1) were mainly calculated based on Thermo-Calc Scheil calculations. As well as a classic Scheil calculation, the Scheil calculator has options to include either back diffusion in the solid, or solute trapping in the primary phase [58], to the authors knowledge, these have not been widely used [61] and a comparison of the 3 calculations has not been published. These are new additions to the software and so have had minimal testing, their reliability is unknown. However, it is interesting to see what behaviour they predict and if rapid solidification conditions are expected to affect the crack susceptibility in both L-PBF and L-DED. Overall (Table 3), the deviation of the new models from the classic Scheil calculation are relatively small, once again, the simplest calculation providing sufficient accuracy for most purposes.

As shown in Table 3, the solute trapping L-PBF (ST PBF) calculation is the most different to the classic Scheil calculation, implying that solute trapping could be affecting the crack susceptibility of these alloys. L-PBF is

expected to experience rapid solidification (non-equilibrium composition) and to be on the cusp of solute trapping. L-DED is an order of magnitude slower so is on the cusp of rapid solidification. Since the ST PBF results are different to the classic Scheil, it can be deduced that solute trapping is predicted to occur at these solidification velocities. The change from classic Scheil to ST DED is much smaller, so solute trapping is unlikely to occur in L-DED, as predicted by literature. These findings increase our confidence in the validity of the new, advanced Scheil solidification simulation. This could be further tested by experimentally finding the threshold scanning speed for solute trapping and comparing this to the solidification curves predicted by Thermo-Calc.

Back diffusion (in the solid) has a larger difference with L-DED cooling rates than with L-PBF. This can be understood when considering the time for diffusion; the quicker cooling rates in L-PBF leads to reduced time at temperature and so less diffusion. The ST PBF calculation leads to a smaller freezing range (Figure 5a), this means that the solidification will occur more quickly and will lead to less segregation. This logically makes sense at the solute trapping will lock atoms in place and reduce compositional variation. On the other hand, back diffusion is expected to occur in the solid in L-DED, diffusion acts to reduce the concentration gradient, so increased back diffusion will lead to less compositional variation. Reduced segregation is expected to reduce the freezing range and as such reduce the susceptibility to solidification cracking – both L-PBF and L-DED have reasons for reduced segregation, hence it's difficult to say that one process is likely to be less susceptible to solidification cracking than the other.

L-DED is typically a hotter process, with larger and more powerful lasers than L-PBF, this typically results in the components experiencing the high temperatures for longer during the hatching. However, in L-PBF, there are often more subsequent hatches in the vicinity, so the effect of reheating may be more significant. An increased time at temperature could increase precipitation and carbide formation, increasing the susceptibility of both liquation cracking and strain-age cracking. As shown by Clare et al [18], some materials are more easily printable using L-PBF whilst others are easier to manufacture using L-DED.

4.3. Printability in L-PBF vs L-DED

Unfortunately, all printability assessments are skewed by research interest, if an alloy is not printable/minimally reported (as defined in [18]), this could either mean that it suffers from failure during manufacture or that it's not industrially relevant, so no prolonged research attempts have been made. The ABD-900AM brochure [24] claims that it is designed to be free of solidification, strain-age and liquation cracks, the calculations above result in susceptibilities $\leqslant 0.7$, so we do not expect these to be prominent. The literature on this alloy used L-PBF [19,24], but as a result of its "exceptional printability" the powder is also advertised for both EB-PBF and L-DED [24]. The implication is since that it is printable in L-PBF, it is printable in all AM processes, which is not an assumption which can be generally made; further experimental evidence regarding this alloy has not yet been reported.

Most development work is done using L-PBF due to the size and cost of the machine. Several trials in L-PBF can be run with as little as 2 kg of powder, which is typically lower than that required for L-DED. In addition, the upfront cost of a L-PBF machine is significantly lower than that for a L-DED or an EB-PBF machine. The fact that tests are conducted on L-PBF machines doesn't necessarily mean that they can be manufactured using other processes.

Since L-DED and L-PBF have very different laser spot sizes and cooling rates, solidification conditions are vastly different. Conduit et al. designed an alloy specifically for L-PBF [20]. Their processability property was extracted by designing a neural network from 10 known compositions. Since the processability will have been tested using L-PBF, their findings are valid for L-PBF, but they do not claim it is suitable for additive manufacturing as a whole. Alloys should be developed specifically with an application and so a manufacturing process in mind. For example, small components with intricate geometries e.g. GE LEAP fuel nozzle, L-PBF is likely the most appropriate process; for larger scale repair applications e.g. blisk repair, L-DED would be used. Once the process is decided,

approximate cooling rates and solidification velocities are known, so an alloy can be better designed to suit the application.

In the wider research community, there is a desire to find a singular value which solves the printability issue. Many of these solutions use dimensionless numbers or compositional analyses (e.g. Figure 1). Similar attempts have been made to define thresholds for keyholing, lack of fusion and other phenomena. Even if we were able to calculate an accurate crack susceptibility, this would vary with the process, geometry, powder composition and the location within the melt pool. An alloy with low crack susceptibility could be developed, but due to the processing conditions chosen, the thermal gradient in a certain part of the melt pool could cause a crack to form.

It seems like a single numeric answer cannot solve such a complex problem; instead, an attempt has been made to assemble a more qualitative metric from simple empirical observations, one which can predict which alloys are likely to have a higher propensity to cracking. This in itself, is a useful metric to have as it gives alloy designers a starting point and a warning as to which failure mechanisms may occur. As more research is conducted on a broader range of compositions, a quantitative printability scale may be developed, allowing for the accuracy of crack susceptibility models to be validated. A standardised printability measure would be needed for this; likely this would consist of either scanning weld tracks or building small, specific geometries and analysing these for cracks.

5. Conclusions

In this paper, several published failure mode susceptibilities were combined in a simple but comprehensive manner. The final overall failure susceptibility is shown to adequately correlate with the printability of alloys reported in literature. The printability of an alloy is difficult to define as a result of the various processes available and the range of processing conditions possible within each. A lack of successful printing reported in literature could either be due to lack of research (insufficient industrial relevance) or due to a high susceptibility of failure (e.g. solidification cracking). As such, the proposed failure susceptibility is a good tool to check the expected printability of an alloy, but is unlikely to be instrumental in development of a new alloy. The proposed method is simpler than currently existing methods, less computationally intensive and requires no prior knowledge of existing materials properties. It's shown that this simpler method provides sufficiently accurate results, limited by experimental measures of printability rather than the calculations themselves.

The difference between L-PBF and L-DED is highlighted thorough the Scheil solidification simulations, with the inclusion of rapid solidification conditions affecting the resultant crack susceptibilities. This confirms the rapid solidification conditions predicted in literature, demonstrating a major difference between L-PBF and L-DED, which is not often reported. For a specific component, the most appropriate process must be decided along with required mechanical properties. Once these guidelines are set, an alloy must be tailored to fit within these and this will result in the best alloy for the specified component. Finally, a standardised measure of printability, using small scale tests is needed to quantify printability for each process.

Acknowledgements

This work was supported by the EPSRC Rolls-Royce Strategic Partnership Grant, MAPP (grant EP/P006566/1) and EPSRC (grant EP/R512175/1). The provision of supporting information from Rolls-Royce plc. is gratefully acknowledged. For the purpose of open access, the author has applied a Creative Commons Attribution (CC BY) licence to any Author Accepted Manuscript version arising.

Author Contributions

LC: Conceptualisation, Methodology, Investigation, Writing – Original Draft. **KAC:** Conceptualisation, Writing – Review & Editing. **LF:** Conceptualisation, Writing – Review & Editing. **MT:** Software, Methodology. **GB:** Conceptualisation. **IT:** Conceptualisation, Writing – Review & Editing, Supervision, Funding

The authors declare that they have no conflict of interest

References

1 W.T. Carter and M.G. Jones: *Proceeding SFF Symp.*, 1993, pp. 51–9.

2 L.N. Carter, M.M. Attallah, and R.C. Reed: *Superalloys 2012*, 2012, pp. 577–86.

3 J.F.S. Markanday: *Mater. Sci. Technol.*, DOI:10.1080/02670836.2022.2068759.

4 H.L. Wei, T. Mukherjee, W. Zhang, J.S. Zuback, G.L. Knapp, A. De, and T. DebRoy: *Prog. Mater. Sci.*, DOI:10.1016/j.pmatsci.2020.100703.

5 T. Mukherjee, J.S. Zuback, A. De, and T. DebRoy: *Sci. Rep.*, 2016, vol. 6, p. 19717.

6 L. Johnson, M. Mahmoudi, B. Zhang, R. Seede, J.T. Maier, H.J. Maier, I. Karaman, and A. Elwany: *Acta Mater.*, 2019, vol. 176, pp. 1–25.

7 American Welding Society (AWS): *Standard Welding Terms and Definitions*, 2010.

8 R.D. Campbell and D.W. Walsh: in *ASM Handbook, Volume 6: Welding, Brazing, and Soldering*, 1993, pp. 603–13.

9 J.N. DuPont, J.C. Lippold, and S.D. Kiser: *Welding Metallurgy and Weldability of Nickel-Base Alloys*, 2009.

10 E.F. Nippes and W.F. Savage: *Weld. J.*, 1949, vol. 28, pp. 534–46.

11 S.D. Kiser: in *ASM Handbook, Volume 6: Welding, Brazing, and Soldering*, 1993.

12 H.N. Moosavy, M.R. Aboutalebi, S.H. Seyedein, M. Khodabakhshi, and C. Mapelli: *Int. J. Miner. Metall. Mater.*, 2013, vol. 20, pp. 1183–91.

13 D. Dye, O. Hunziker, and R.C. Reed: *Acta Mater.*, 2001, vol. 49, pp. 683–97.

14 N.L. Richards and M.C. Chaturvedi: *Int. Mater. Rev.*, 2000, vol. 45, pp. 109–29.

15 M. Durand-Charre: *The Microstructure of Superalloys*, Gordon and Breach Science Publishers, 1997.

16 M.J. Donachie and S.J. Donachie: *Superalloys: A Technical Guide*, 2nd edn., ASM International, 2002.

17 R.C. Reed: *The Superalloys Fundamentals and Applications*, vol. 9780521859042, 2006.

18 A.T. Clare, R.S. Mishra, M. Merklein, H. Tan, I. Todd, L. Chechik, J. Li, and M. Bambach: *J. Mater. Process. Technol.*, DOI:10.1016/j.jmatprotec.2021.117358.

19 Y.T. Tang, C. Panwisawas, J.N. Ghoussoub, Y. Gong, J.W.G. Clark, A.A.N. Németh, D.G. McCartney, and R.C. Reed: *Acta Mater.*, 2021, vol. 202, pp. 417–36.

20 B.D. Conduit, T. Illston, S. Baker, D.V. Duggappa, S. Harding, H.J. Stone, and G.J. Conduit: *Mater. Des.*, 2019, vol. 168, p. 107644.

21 M.M. Attallah, R. Jennings, X. Wang, and L.N. Carter: *MRS Bull.*, 2016, vol. 41, pp. 758–64.

22 H. Naffakh Moosavy, M.R. Aboutalebi, S.H. Seyedein, and C. Mapelli: *Mater. Charact.*, 2013, vol. 82, pp. 41–9.

23 Q. Han, R. Mertens, M.L. Montero-Sistiaga, S. Yang, R. Setchi, K. Vanmeensel, B. Van Hooreweder, S.L. Evans, and H. Fan: *Mater. Sci. Eng. A*, 2018, vol. 732, pp. 228–39.

24 *Oxmet Technol.*, 2021.

25 T.M. Pollock, A.J. Clarke, and S.S. Babu: *Metall. Mater. Trans. A Phys. Metall. Mater. Sci.*, 2020, vol. 51, pp. 6000–19.

26 M.C. Hardy, C. Argyrakis, H.S. Kitaguchi, A.S. Wilson, R.C. Buckingham, K. Severs, S. Yu, C. Jackson, E.J. Pickering, S.C.H. Llewelyn, C. Papadaki, K.A. Christofidou, P.M. Mignanelli, A. Evans, D.J. Child, H.Y. Li, N.G. Jones, C.M.F. Rae, P. Bowen, and H.J. Stone: *Proc. 14th Int. Symp. Superalloys*, DOI:10.1007/978-3-030-51834-9_2 This.

27 H. International: *Haynes Int.*

28 ATI: 2013, vol. 1, pp. 1–5.

29 T. Illston: *Int. Conf. Addit. Manuf. 2012*, 2012.

30 M.H. Haafkens and J.H.G. Matthey: in *Maintenance in Service of High Termperature Parts. Agard Conference Proceedings No. 317*, vol. 317, 1981.

31 B. Wahlmann, D. Leidel, M. Markl, and C. Körner: .

32 N. Kwabena Adomako, N. Haghdadi, and S. Primig: *Mater. Des.*, 2022, vol. 223, p. 111245.

33 S. Catchpole-Smith, N. Aboulkhair, L. Parry, C. Tuck, I.A. Ashcroft, and A. Clare: *Addit. Manuf.*, 2017, vol. 15, pp. 113–22.

34 M.B. Henderson, D. Arrell, R. Larsson, M. Heobel, and G. Marchant: *Sci. Technol. Weld. Join.*, 2004, vol. 9, pp. 13–21.

35 S. Kou: *Acta Mater.*, 2015, vol. 88, pp. 366–74.

36 N. Wang, S. Mokadem, M. Rappaz, and W. Kurz: *Acta Mater.*, 2004, vol. 52, pp. 3173–82.

37 D.G. Eskin and L. Katgerman: *Metall. Mater. Trans. A Phys. Metall. Mater. Sci.*, 2007, vol. 38 A, pp. 1511–9.

38 N. Coniglio and C.E. Cross: *Int. Mater. Rev.*, 2013, vol. 58, pp. 375–97.

39 T.W. Clyne and G.J. Davies: in *Solidification and Casting of Metals*, Sheffield, 1977, pp. 275–8.

40 M. Rappaz, J.-M. Drezet, and M. Gremaud: *Metall. Mater. Trans. A*, 1999, vol. 30, pp. 449–55.

41 E.A. Ott, J. Groh, and H. Sizek: *Proc. Int. Symp. Superalloys Var. Deriv.*, 2005, pp. 35–45.

42 L.N. Carter, C. Martin, P.J. Withers, and M.M. Attallah: *J. Alloys Compd.*, 2014, vol. 615, pp. 338–47.

43 G.A. Young, T.E. Capobianco, M. a. Penik, B.W. Morris, and J.J. McGee: *Weld. J.*, 2008, vol. 87, pp. 31S-43S.

44 C.T. Sims, N.S. Stoloff, and W.C. Hagel: *Superalloys II: High-Temperature Materials for Aerospace and Industrial Power*, John Wiley & Sons, 1987.

45 T. DebRoy, H.L. Wei, J.S. Zuback, T. Mukherjee, J.W. Elmer, J.O. Milewski, A.M. Beese, A. Wilson-Heid, A. De, and W. Zhang: *Prog. Mater. Sci.*, 2018, vol. 92, pp. 112–224.

46 W. Kurz and R. Trivedi: *Mater. Sci. Eng. A*, 1994, vol. 179–180, pp. 46–51.

47 R. Deffley: University of Sheffield, 2012.

48 J. Hunt, F. Derguti, and I. Todd: *Ironmak. Steelmak.*, 2014, vol. 41, pp. 254–6.

49 R.L. Dreshfield: *NASA Tech. Note*.

50 H.J. Murphy, C.T. Sims, and A.M. Beltran: *Superalloys 1968*, 1968, pp. 47–66.

51 C.L. Frederick: 2018, pp. 1–143.

52 F. Tancret and H.K.D.H. Bhadeshia: *Mater. Sci. Technol.*, 2003, vol. 19, p. 291.

53 R.C. Reed, T. Tao, and N. Warnken: *Acta Mater.*, 2009, vol. 57, pp. 5898–913.

54 M.A. Charpagne, K. V. Vamsi, Y.M. Eggeler, S.P. Murray, C. Frey, S.K. Kolli, and T.M. Pollock: *Acta Mater.*, 2020, vol. 194, pp. 224–35.

55 S.P. Murray, K.M. Pusch, A.T. Polonsky, C.J. Torbet, G.G.E. Seward, N. Zhou, S.A.J. Forsik, P. Nandwana, M.M. Kirka, R.R. Dehoff, W.E. Slye, and T.M. Pollock: *Nat. Commun.*, 2020, vol. 11, pp. 1–11.

56 T.M. Smith, A.C. Thompson, T.P. Gabb, C.L. Bowman, and C.A. Kantzos: *Sci. Rep.*, 2020, vol. 10, pp. 1–9.

57 F. Markanday, G. Conduit, B. Conduit, J. Pürstl, K. Christofidou, L. Chechik, G. Baxter, C. Heason, and H. Stone: *Data-Centric Eng.*, DOI:10.1017/dce.2022.31.

58 J.O. Andersson, T. Helander, L. Höglund, P. Shi, and B. Sundman: *Calphad Comput. Coupling Phase Diagrams Thermochem.*, 2002, vol. 26, pp. 273–312.

59 J.N. Ghoussoub, Y.T. Tang, W.J.B. Dick-Cleland, A.A.N. Németh, Y. Gong, D.G. McCartney, A.C.F. Cocks, and R.C. Reed: *Metall. Mater. Trans. A Phys. Metall. Mater. Sci.*, 2022, vol. 53, pp. 962–83.

60 S. Griffiths, H. Ghasemi Tabasi, T. Ivas, X. Maeder, A. De Luca, K. Zweiacker, R. Wróbel, J. Jhabvala, R.E. Logé, and C. Leinenbach: *Addit. Manuf.*, DOI:10.1016/j.addma.2020.101443.

61 J. Xu, P. Kontis, R.L. Peng, and J. Moverare: *Acta Mater.*, 2022, vol. 240, p. 118307.

62 N. Zhou, A.D. Dicus, S.A.J. Forsik, T. Wang, G.A. Colombo, and M.E. Epler: in *Superalloys 2020*, Springer International Publishing, 2020, pp. 1046–54.

63 J.U. Park, S.Y. Jun, B.H. Lee, J.H. Jang, B.S. Lee, H.J. Lee, J.H. Lee, and H.U. Hong: *Addit. Manuf.*, 2022, vol. 52, p. 102680.

64 H. Yu, J. Liang, Z. Bi, J. Li, and W. Xu: *Metall. Mater. Trans. A Phys. Metall. Mater. Sci.*, 2022, vol. 53, pp. 1945–54.

65 *Calculation of Electron Vacancy Number in Superalloys*, SAE International, 2017.

66 M. Morinaga, N. Yukawa, H. Adachi, and H. Ezaki: *Superalloys 1984 (Fifth Int. Symp.*, 1984, pp. 523–32.

67 Y. Sato: *Jpn. J. Appl. Phys.*, 2011, vol. 50, pp. 15–8.

68 Y. Sato, K. Sugisawa, D. Aoki, and T. Yamamura: *17th Eur. Conf. Thermophys. Prop.*, 2005, pp. 1–5.

69 D. Liu, J.C. Lippold, J. Li, S.R. Rohklin, J. Vollbrecht, and R. Grylls: *Metall. Mater. Trans. A Phys. Metall. Mater. Sci.*, 2014, vol. 45, pp. 4454–69.

70 A.J. Pinkerton, M. Karadge, W. Ul Haq Syed, and L. Li: *J. Laser Appl.*, 2006, vol. 18, pp. 216–26.

71 K.A. Mumtaz, P. Erasenthiran, and N. Hopkinson: *J. Mater. Process. Technol.*, 2008, vol. 195, pp. 77–87.

Appendix

Table A I: Raw susceptibilities for the 10 susceptibilities for each of the 21 alloys

Alloy	HT1	HT2	HT3	HT4	TCP1	TCP2	TCP3	SAC1	SAC2	SAC3	LC1
Inconel 718	0.30	173.0	1302	0.51	2.28	0.88	0.92	1.26	2.48	2	5.32
Inconel 625	0.91	201.8	1444	0.52	2.06	0.89	0.91	0.37	1.38	0	6.02
Hastelloy X	1.04	77.6	478	0.49	2.52	0.93	0.94	2.00	2.00	0	6.22
Waspaloy	1.40	275.3	1499	0.53	2.21	0.89	0.94	3.92	3.13	23	6.04
CM247LC	1.95	225.5	1037	0.53	2.06	0.90	0.98	6.19	6.43	69	2.63
CMSX-4	1.20	176.4	1090	0.52	1.95	0.87	0.97	6.44	7.08	68	2.21
ABD-850AM	1.16	334.4	2530	0.52	2.14	0.88	0.92	3.15	2.65	21	5.99
ABD-900AM	0.63	298.9	2177	0.52	2.29	0.89	0.95	4.12	4.05	30	5.61
AlloyDLD	1.30	253.9	1611	0.51	2.11	0.89	0.94	2.90	3.80	26	5.49
Rene41	0.88	198.9	1102	0.51	2.29	0.92	0.96	4.10	3.05	26	5.79
In738	1.70	279.5	1728	0.52	2.26	0.90	0.98	6.26	5.70	49	4.85
In713LC	1.74	205.9	1017	0.52	2.10	0.90	0.97	6.50	6.90	80	3.36
Udimet700	0.94	230.3	1930	0.53	2.55	0.92	0.99	7.19	6.00	57	5.00
RR1000	1.64	441.4	1754	0.53	2.45	0.91	0.98	6.02	5.10	43	5.00
Inconel939	1.26	334.8	1509	0.52	2.46	0.90	0.96	5.01	4.05	32	7.09
Haynes282	1.24	216.1	869	0.51	2.22	0.90	0.94	3.26	2.55	20	6.03
Udimet720	0.89	249.1	735	0.52	2.46	0.91	1.01	6.70	5.00	44	5.64
718+	0.39	216.3	645	0.52	2.51	0.88	0.91	2.92	3.98	26	5.71

683 *Table A II: Normalised susceptibilities for the 10 susceptibilities for each of the 21 alloys*

Deviation from Scheil Calculation

Alloy	HT1	HT2	HT3	HT4	TCP1	TCP2	TCP3	SAC1	SAC2	SAC3	LC1
Inconel 718	0.00	0.26	0.40	0.61	0.56	0.14	0.18	0.13	0.19	0.02	0.64
Inconel 625	0.37	0.34	0.47	0.42	0.19	0.34	0.08	0.00	0.00	0.00	0.78
Hastelloy X	0.45	0.00	0.00	1.00	0.94	1.00	0.35	0.24	0.11	0.00	0.82
Waspaloy	0.66	0.54	0.50	0.04	0.44	0.21	0.35	0.52	0.31	0.29	0.79
CM247LC	1.00	0.41	0.27	0.00	0.18	0.42	0.77	0.85	0.89	0.86	0.09
CMSX-4	0.55	0.27	0.30	0.39	0.00	0.00	0.66	0.89	1.00	0.86	0.00
ABD-850AM	0.52	0.71	1.00	0.35	0.32	0.11	0.18	0.41	0.22	0.26	0.77
ABD-900AM	0.20	0.61	0.83	0.24	0.56	0.27	0.45	0.55	0.47	0.38	0.70
AlloyDLD	0.60	0.48	0.55	0.55	0.28	0.31	0.31	0.37	0.42	0.32	0.67
Rene41	0.35	0.33	0.30	0.60	0.57	0.81	0.54	0.55	0.29	0.33	0.73
In738	0.85	0.55	0.61	0.23	0.52	0.42	0.71	0.86	0.76	0.61	0.54
In713LC	0.87	0.35	0.26	0.25	0.25	0.48	0.67	0.90	0.97	1.00	0.24
Udimet700	0.39	0.42	0.71	0.18	1.00	0.90	0.80	1.00	0.81	0.71	0.57
RR1000	0.81	1.00	0.62	0.20	0.83	0.72	0.72	0.83	0.65	0.54	0.57
Inconel939	0.58	0.71	0.50	0.43	0.86	0.49	0.55	0.68	0.47	0.40	1.00
Haynes282	0.57	0.38	0.19	0.59	0.46	0.55	0.33	0.42	0.21	0.25	0.78
Udimet720	0.36	0.47	0.12	0.27	0.85	0.64	1.00	0.93	0.64	0.55	0.70
718+	0.05	0.38	0.08	0.38	0.94	0.01	0.00	0.37	0.46	0.33	0.72

684

685

686

687

688

689

690 *Table A III: Comparison of different Thermo-Calc Scheil calculations for the main alloys being analysed. Shown are the results*
691 *of the classic Scheil calculation along with Back Diffusion calculations and the Solute Trapping calculation - for both L-PBF and*
692 *L-DED. The percentage differences compared to the classic Scheil calculation are shown*

Material	Calculation	Freezing Range	Crack Susceptibility Coefficient	Kou Cracking Susceptibility	Freezing Range	Crack Susceptibility Coefficient	Kou Cracking Susceptibility
Inconel 718	Scheil	173.0	0.30	1301.9	N/A	N/A	N/A
Inconel 625	Scheil	201.8	0.91	1444.1	N/A	N/A	N/A
Hastelloy X	Scheil	77.6	1.04	478.4	N/A	N/A	N/A
Waspaloy	Scheil	275.3	1.40	1499.1	N/A	N/A	N/A
CM247LC	Scheil	225.5	1.95	1036.6	N/A	N/A	N/A
CMSX-4	Scheil	176.4	1.20	1090.5	N/A	N/A	N/A
ABD-850AM	Scheil	334.4	1.16	2529.8	N/A	N/A	N/A
ABD-900AM	Scheil	298.9	0.63	2177.1	N/A	N/A	N/A
AlloyDLD	Scheil	253.9	1.30	1610.9	N/A	N/A	N/A
Inconel 718	BD PBF	173.0	0.30	1301.5	0.00	0.00	0.00
Inconel 625	BD PBF	201.8	0.90	1446.6	0.00	-0.01	0.00
Hastelloy X	BD PBF	68.4	0.79	442.6	-0.12	-0.23	-0.07
Waspaloy	BD PBF	275.1	1.38	1491.8	0.00	-0.01	0.00
CM247LC	BD PBF	222.8	1.91	1034.1	-0.01	-0.02	0.00
CMSX-4	BD PBF	175.1	1.19	1079.3	-0.01	-0.01	-0.01
ABD-850AM	BD PBF	333.3	1.16	2547.2	0.00	0.00	0.01
ABD-900AM	BD PBF	298.8	0.62	2173.4	0.00	0.00	0.00
AlloyDLD	BD PBF	254.0	1.29	1619.6	0.00	0.00	0.01
Inconel 718	ST PBF	164.9	0.91	1374.0	-0.05	2.02	0.06
Inconel 625	ST PBF	201.4	0.92	1412.7	0.00	0.02	-0.02
Hastelloy X	ST PBF	69.2	1.43	350.0	-0.11	0.38	-0.27
Waspaloy	ST PBF	225.3	1.36	1074.3	-0.18	-0.02	-0.28
CM247LC	ST PBF	182.0	1.73	929.1	-0.19	-0.11	-0.10
CMSX-4	ST PBF	162.4	1.36	953.5	-0.08	0.13	-0.13
ABD-850AM	ST PBF	296.5	1.65	1981.7	-0.11	0.42	-0.22
ABD-900AM	ST PBF	298.8	0.62	2173.4	0.00	0.00	0.00
AlloyDLD	ST PBF	237.6	1.64	1356.7	-0.06	0.26	-0.16
Inconel 718	BD DED	173.0	0.30	1301.1	0.00	0.01	0.00
Inconel 625	BD DED	201.9	0.87	1460.4	0.00	-0.04	0.01
Hastelloy X	BD DED	63.8	0.74	388.4	-0.18	-0.29	-0.19
Waspaloy	BD DED	274.0	1.33	1466.8	0.00	-0.05	-0.02
CM247LC	BD DED	213.6	1.76	1024.7	-0.05	-0.10	-0.01
CMSX-4	BD DED	169.0	1.13	1025.9	-0.04	-0.06	-0.06
ABD-850AM	BD DED	333.1	1.17	2561.0	0.00	0.01	0.01
ABD-900AM	BD DED	298.5	0.62	2164.9	0.00	-0.01	-0.01
AlloyDLD	BD DED	254.0	1.26	1626.9	0.00	-0.03	0.01
Inconel 718	ST DED	172.0	0.32	1326.2	-0.01	0.07	0.02
Inconel 625	ST DED	196.6	1.26	971.2	-0.03	0.39	-0.33
Hastelloy X	ST DED	77.6	1.07	470.6	0.00	0.03	-0.02
Waspaloy	ST DED	272.7	1.40	1510.7	-0.01	0.00	0.01

CM247LC	ST DED	222.4	1.93	1029.9	-0.01	-0.01	-0.01
CMSX-4	ST DED	176.0	1.21	1084.6	0.00	0.01	-0.01
ABD-850AM	ST DED	326.5	1.15	2551.6	-0.02	-0.01	0.01
ABD-900AM	ST DED	296.9	0.64	2237.5	-0.01	0.02	0.03
AlloyDLD	ST DED	253.5	1.33	1594.9	0.00	0.03	-0.01

693